Journal of
Synchrotron Radiation

ISSN 0909-0495

Received 1 March 2009
Accepted 24 July 2009

Confocal full-field X-ray microscope for novel three-dimensional X-ray imaging

Akihisa Takeuchi,[a]* Yasuko Terada,[a] Yoshio Suzuki,[a] Kentaro Uesugi[a] and Sadao Aoki[b]

[a]SPring-8/Japan Synchrotron Radiation Research Institutes (JASRI), Hyogo 679-5198, Japan, and [b]Graduate School of Pure and Applied Sciences, University of Tsukuba, Ibaraki 305-8573, Japan. E-mail: take@spring8.or.jp

A confocal full-field X-ray microscope has been developed for use as a novel three-dimensional X-ray imaging method. The system consists of an X-ray illuminating 'sheet-beam' whose beam shape is micrified only in one dimension, and an X-ray full-field microscope whose optical axis is normal to the illuminating sheet beam. An arbitral cross-sectional region of the object is irradiated by the sheet-beam, and secondary X-ray emission such as fluorescent X-rays from this region is imaged simultaneously using the full-field microscope. This system enables a virtual sliced image of a specimen to be obtained as a two-dimensional magnified image, and three-dimensional observation is available only by a linear translation of the object along the optical axis of the full-field microscope. A feasibility test has been carried out at beamline 37XU of SPring-8. Observation of the three-dimensional distribution of metallic inclusions in an artificial diamond was performed.

Keywords: three-dimensional imaging; secondary X-ray emission; fluorescent X-ray; confocal; full-field X-ray microscope.

1. Introduction

X-ray computed tomography (CT) is a powerful measuring method which enables non-destructive three-dimensional spatial observation of inner structures of materials. Three-dimensional diagnostics using X-ray CT, which was originally developed for medical use, is now widely required in various other fields. Therefore, various types of three-dimensional X-ray imaging methods specialized for each purpose have been proposed, such as micro/nanotomography, phase-contrast tomography, three-dimensional X-ray diffraction (3D-XRD), three-dimensional X-ray fluorescence and/or X-ray scattering imaging (3D-XRF/XRS).

3D-XRF/XRS, which requires the secondary X-ray emission imaging technique, has so far been available only with scanning-microscopy-based X-ray CT [Fig. 1(*a*); Golosio *et al.*, 2004]. However, more recently, some other three-dimensional imaging methods that overcome the disadvantages of the conventional CT method have been proposed. The confocal scanning X-ray microscope (CSXM) system using poly-capillary optics, as shown in Fig. 1(*b*), allows only an arbitrary three-dimensional part of an object to be investigated (Kanngießer *et al.*, 2003; Vekemans *et al.*, 2004), while conventional CT inherently requires measuring the whole body of an object even if the region of interest is only a fraction. On the other hand, a full-field fluorescent X-ray microscope which enables secondary X-ray emission to be observed as a two-dimensional magnified image has been developed (Aoki *et al.*, 1998; Takeuchi *et al.*, 2000), and has been applied to the CT system [Fig. 1(*c*); Watanabe *et al.*, 2001; Ohigashi *et al.*, 2004; Hoshino *et al.*, 2007]. This system has the advantage of high throughput because three-dimensional observation is available with only a rotation scan, while scanning-microscopy-based CT requires an additional two-dimensional raster scan.

In this paper a novel three-dimensional X-ray imaging method for secondary X-ray emission is proposed, which combines both advantages of the aforementioned full-field microscope system and confocal system. The system consists of an illuminating 'sheet-beam' whose beam shape is micrified only in one dimension and therefore has a sheet-like-shaped optical path, and a full-field X-ray microscope system whose optical axis is set to be normal to the illuminating sheet-beam. Secondary X-ray emission such as fluorescent X-rays and scattering X-rays is imaged simultaneously with the full-field microscope. Because only an arbitral cross-sectional region of the object is irradiated with the sheet-beam, a virtual sliced image of the object can be observed. Since the relation between the optical path of the illuminating sheet-beam and the object plane of the full-field microscope is confocal, this system may be called a confocal full-field X-ray microscope (CFXM) of orthogonal geometry. In this paper, details of this system will be presented. A 3D-XRF image of metallic inclusions in an artificial diamond will be shown. Energy-

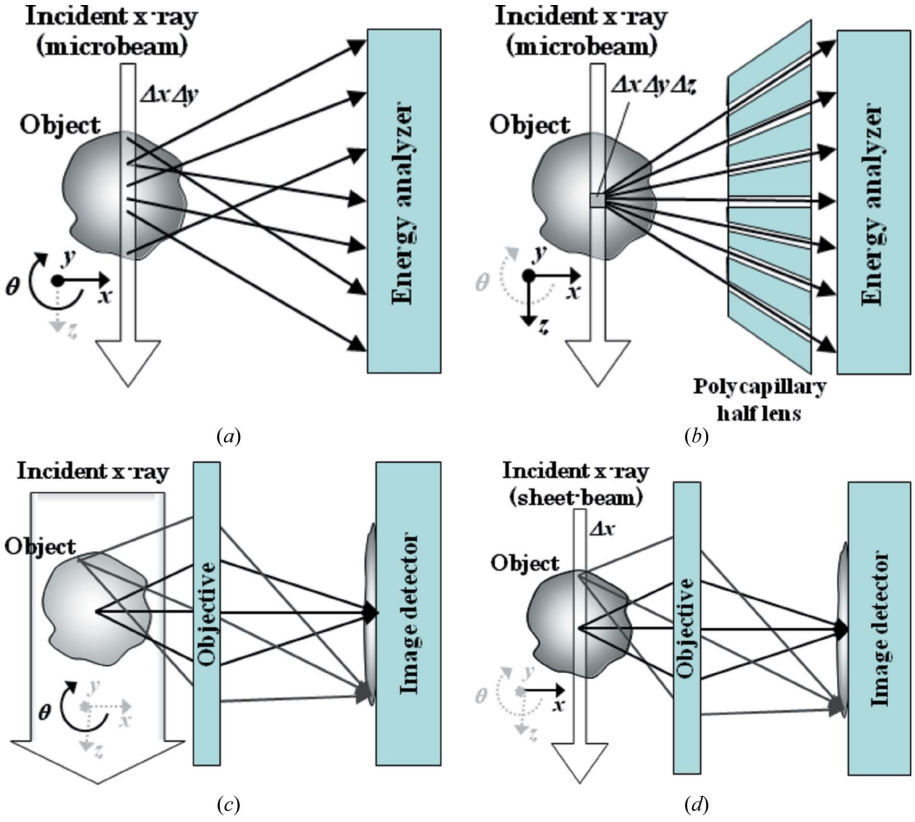

Figure 1
Conceptual diagrams of the optical systems for three-dimensional X-ray fluorescence imaging. (*a*) Scanning microscope CT, (*b*) confocal scanning microscope, (*c*) full-field microscope CT, and (*d*) confocal full-field microscope. The object is located at the origin of the Cartesian coordinate system *x*–*y*–*z*. Incident X-rays travel along the *z*-axis. The directions of the *x*- and *y*-axes are perpendicular to the *z*-axis in the horizontal plane and the vertical direction, respectively. The optical axis of the X-ray fluorescence detecting system points to the origin along the *x*-axis. The scan direction that each method needs for three-dimensional imaging is shown as black characters and black arrows.

resolved 3D-XRF using a CCD camera as an energy-dispersible X-ray imager will also be shown.

2. Confocal full-field X-ray microscope system

A conceptual diagram of the CFXM optics is shown in Fig. 1(*d*). Let us take a Cartesian coordinate system *x*–*y*–*z* with its origin in the object. Consider *x*, *y* and *z* as the horizontal direction, vertical direction and the direction of optical axis of the incident beam from the light source, respectively. The optical axis of the full-field X-ray microscope is coincident with the *x*-axis, and its object plane is aligned to coincide with the *y*–*z* plane including the origin. In this situation, if the whole body of the object is illuminated, secondary X-ray emission from the object is observed as a two-dimensional (*y*–*z*) image at the image plane (the situation is just the same as in Fig. 1*c*). However, the obtained image has no spatial information in the *x*-direction because typical X-ray microscope optics have a very large depth of focus. Then, if only the *x*-directional width of the illuminating beam is very small (Δx), only a cross-sectional region of the object of width Δx at the *y*–*z* plane is illuminated. Therefore, the obtained image corresponds to a two-dimensional emission distribution from this cross-sectional region. In this manner, the spatial resolution in the *y*–*z* plane is determined with that of the full-field X-ray microscope system, and its depth resolution is independently determined by the *x*-directional width of the illuminating beam Δx. A three-dimensional image data set is simply obtained by an *x*-directional translation scanning of the object. A three-dimensional image is reconstructed by simply stacking these sequential sliced image data if self-absorbtion is negligible. When the self-absorption is not negligible, the absorption coefficient distribution in the object must be measured separately. The influence of multiple excited fluorescent X-rays is just the same as in other methods such as using full-field microscope optics. The precise estimation of the influence of multiple excited fluorescent X-rays in full-field microscope optics has been described elsewhere (Ohigashi *et al.*, 2006).

Comparing the CFXM with conventional CT as a three-dimensional X-ray imaging method, the advantages of the CFXM are as follows: (i) an arbitrary virtual sliced image can be directory observed with one-shot acquisition; (ii) therefore, an arbitral small portion of relatively large sample can be observed whereas conventional CT requires measuring the whole body of the sample, and (iii) no image-reconstruction processes are required. Since a CFXM is based on a confocal optics and a full-field microscope, this system has similar characteristics to both of them, and the first characteristic is peculiar to the CFXM.

Because secondary X-ray emissions are usually polychromatic beams which include elastic (Thomson) scattering, inelastic (Compton) scattering and some fluorescent X-ray lines, it is preferable for the full-field microscope optics to be achromatic. The microscope system is also required to have a large acceptance and a high efficiency for high throughput. From these points of view, total reflection mirror optics are preferable for the objective. In particular, Wolter-type total-reflection mirrors are one of the most suitable objectives for this purpose because they have a much larger (typically about 10^2 times) angular aperture than other typical X-ray objective devices such as Fresnel zone plates and refractive lenses. Although pinhole-camera systems and parallel optics using X-ray collimators are also achromatic, their acceptance is much smaller than that of the typical X-ray objectives, especially for high-resolution imaging, because the spatial resolutions are determined by the hole size.

Three-dimensional elemental mapping is also possible by using techniques that have been attempted in previous

Table 1
Typical parameters of the one-dimensional focusing mirror.

Material	Platinum-coated fused quartz
Surface figure	Plane parabola
Focal length	400 mm
Averaged glancing angle	2.8 mrad
Aperture	507 μm
Length	190 mm
Width	20 mm
Thickness	15 mm
Reflectivity at 10 keV	0.87

experiments: *i.e.* the absorption-edge subtraction method (Yamamoto *et al.*, 2000*a*,*b*), and fluorescent X-ray analysis with an energy-dispersive X-ray imaging detector (Ohigashi *et al.*, 2002, 2004; Hoshino *et al.*, 2007).

3. Experimental set-up

The experiment was carried out at the undulator beamline BL37XU of SPring-8. A schematic diagram of the CFXM experimental set-up is shown in Fig. 2. The system was constructed at experimental hutch 1. Details of BL37XU are described elsewhere (Terada *et al.*, 2004). Because the incident beam from the undulator light source is linearly polarized in the horizontal direction, almost no X-ray scattering is observed with this arrangement. The photon energy of the illuminating X-rays was set to be 10 keV by passing through a Si 111 double-crystal monochromator.

In order to generate a sheet-beam, a one-dimensional focusing total reflection mirror was installed in the horizontal focusing configuration. Since the depth of focus is very large, a line-focused beam can be approximated as a sheet-beam. Typical parameters of the mirror are shown in Table 1. This mirror was fabricated by Canon, Japan, using the bent-polishing method (Takeuchi *et al.*, 2005). The dimensions of the incident beam onto the one-dimensional mirror were 0.5 mm (horizontal; x-direction) × 1 mm (vertical; y-direction). Although the achievable focal spot size of this mirror is 1.5 μm (Suzuki *et al.*, 2008), the focal spot size full width at half maximum (FWHM) for this experiment was set to be 10 μm by intentionally misaligning the tilt angle. Therefore, the line-focused beam dimensions were approximately 10 μm (x) × 1 mm (y). The depth of focus was approximately 8 mm (z). The maximum photon flux of the line-focused beam was measured to be approximately 1.5×10^{12} photons s^{-1} (therefore, the flux density at the object plane was 1.5×10^{8} photons s^{-1} μm^{-2}). Full-field X-ray imaging microscope optics were set to be normal to the incident beam in the horizontal plane. The microscope system consisted of a Wolter-type total reflection mirror as the objective and a direct-sensing-type CCD camera as the image detector. Typical parameters of the Wolter mirror are shown in Table 2. The mirror was fabricated by Nikon, Japan, using the 'glass replica' method (Onuki *et al.*, 1992). The spatial resolution of the microscope system was estimated from the edge response of a test sample image. A 20 μm-thick copper foil was used as the test sample, and the measured spatial resolution was approximately 10 μm. This value is consistent with the previous experiment (Yamamoto *et al.*, 2000*a*). The parameters of the CCD camera (c4880-50-24, Hamamatsu Photonics, Japan) are shown in Table 3. Since the readout time of the CCD is about 3.5 s per frame, a mechanical X-ray shutter was installed upstream of the one-dimensional focusing mirror in order to prevent the error-detection of X-rays during such a long readout time. The time response of the shutter was about 1 s, which determined the shortest exposure time. The CCD camera was used as an energy-dispersible X-ray imager by operating under the photon-counting mode, as well as simply used as an image detector (Tsunemi *et al.*, 1991). In this measuring mode the illuminating photon flux was intentionally decreased to be about 1/40 of maximum intensity in order to satisfy the single-event condition of the CCD camera with 1 s exposure. The measured energy resolution was approximately 200 eV.

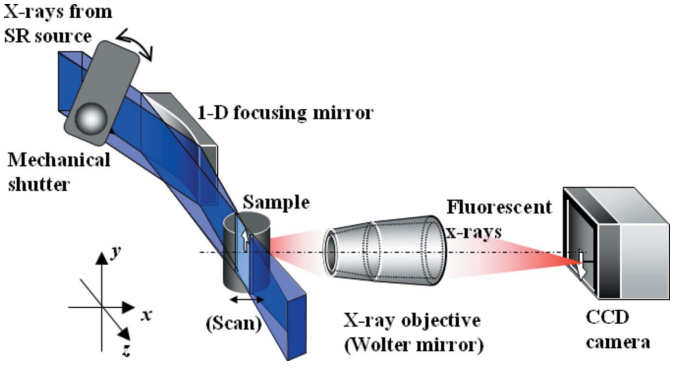

Figure 2
Schematic diagram of the experimental set-up of the confocal full-field X-ray microscope.

Table 2
Typical parameters of the Wolter-type total reflection mirror objective.

Material	Platinum-coated Pyrex glass
Surface figure	Tandem of hyperboloid and ellipsoid
Averaged glancing angle	7 mrad
Numerical aperture	2.7×10^{-2}
Solid angle of aperture	2.4×10^{-4} sterad
Length	35 mm + 35 mm
Object–image distance	2654.6 mm
Magnification	×13
Total reflectivity at Cu $K\alpha$	∼0.7

Table 3
Typical parameters of the direct-sensing-type CCD camera.

Data transfer system	Full-frame transfer
Cooling system	Air-cooling with Peltier device
Device temperature	223 K
Pixel format	1000 (h) × 1018 (v)
Pixel size (normal)	13 μm
Frame rate	0.29 frames s^{-1}
A/D conversion	14-bit

The distance between the object plane and the detector at the image plane was set to be about 2650 mm. Magnification of the X-ray microscope system was ∼13. The X-ray path between the Wolter mirror and the CCD camera was evacuated. The CCD camera was used under the 2 × 2 or 4 × 4 binning mode; therefore, in each case, the converted pixel size

at the sample position was about 2 μm or 4 μm, respectively. The translation step in the x-direction of the sample was adjusted to that of the converted pixel size in each case. Because both the width of the sheet-beam and the spatial resolution of the microscope system were approximately 10 μm, the three-dimensional spatial resolution of this system was approximately 10 μm × 10 μm × 10 μm in FWHM. As a typical example, the image intensity of Fe $K\alpha$ from a pure iron bulk sample (density 7.86 g cm^{-3}) was measured, and the counting rate was about 10 photons s^{-1} pixel^{-1} with 2 × 2 binning mode (corresponding voxel size: 10 μm × 2 μm × 2 μm). Considering the absorption effect and the spatial resolution of the present system, the sensitivity is estimated to be of the order of a few tens of photons ng^{-1} s^{-1}.

4. Results and discussion

A feasibility test of the CFXM was performed using an artificial diamond as the sample. The diamond was fabricated using the 'solvent method', and metallic inclusions such as Fe, Co and Ni used as the solvent for the crystal growth are distributed. They form numerous small particles and are arrayed along internal boundaries between crystal growth regions. Particle size is typically 1–10 μm in diameter, and the content rate of the metals in each particle is about 90 wt% (Wakatsuki, 1984). Fig. 3 shows a cross-sectional image in the y–z plane of the sample. Because the image was obtained at a scattering angle of 90°, only fluorescent X-rays from the metallic inclusions are recognized, while neither scattering nor fluorescent X-ray emission from the carbon crystal is seen. Fig. 4 shows three-dimensional rendered images of the sample. Figs. 4(*a*), 4(*b*) and 4(*c*) represent the front view (y–z), side view (x–y) and top view (z–x), respectively. The image data set consists of a sequential series of 350 sliced images recorded by translating the sample in the x-direction. It can be seen that the metal inclusions are distributed radially in three dimensions. Here, no compensation for absorption and secondary excited fluorescent X-rays are made. The measured count rate of the sliced image is about 4 photons s^{-1} (2 × 2 binning pixel)$^{-1}$. However, the measured value might be undercounted since the particle sizes are almost the same as the spatial resolution. For the same reason, the shapes and inside structures of the particles were not resolved while the distributions of particles were observed

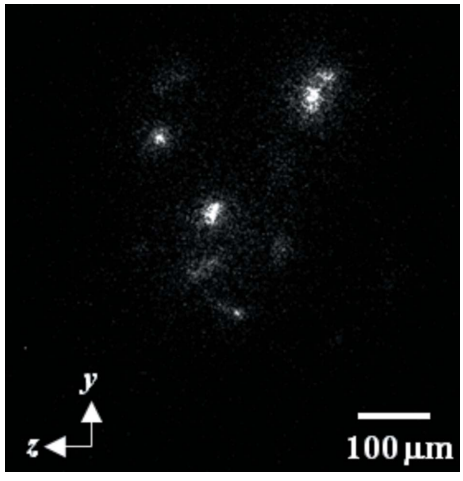

Figure 3
Virtual cross-sectional X-ray fluorescence image of artificial diamond containing metallic inclusions (Fe, Co, Ni). The incident X-ray energy was 10 keV and the exposure time was 8 s. The pixel size of the image is 2 μm × 2 μm (2 × 2 binning mode), and the number of pixels is 512 × 512.

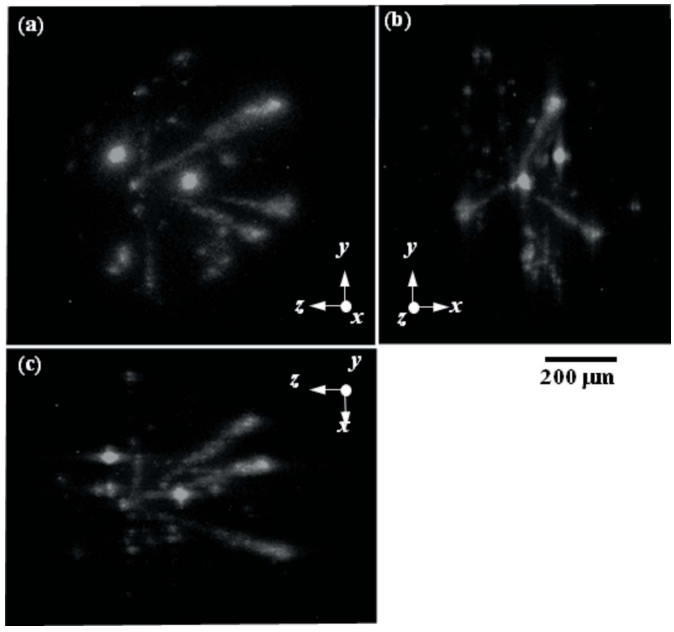

Figure 4
Rendered images of three-dimensional X-ray fluorescence emission distribution from the artificial diamond. (*a*) Front view (y–z), (*b*) side view (x–y) and (*c*) top view (z–x). The three-dimensional data set consists of 350 cross-sectional images as shown in Fig. 3. The exposure time of each cross-sectional image was 8 s. The translation scan pitch of the sample was 2 mm. The voxel size is 2 mm × 2 mm × 2 mm, and the number of voxels is 350 (x) × 512 (y) × 512 (z). The total measurement time was ∼75 min.

Three-dimensional elemental mapping of the metallic inclusions was also tested using the energy-dispersible imaging mode of the CCD camera (for details, see Hoshino *et al.*, 2007; Ohigashi *et al.*, 2002). Because the statistics of a single photon-counting image are not high enough for the image contrast, 300 photon-counting images were repeatedly acquired in order to increase the statistics. Figs. 5(*a*) and 5(*b*) show volume rendering images representing the three-dimensional distributions of Fe and Co, respectively, and Fig. 5(*c*) shows the X-ray spectrum derived from the histogram of all of the image data set. Comparing images Fig. 5(*a*) and 5(*b*), almost no difference in elemental distribution between the Fe image and the Co image is seen. Although the elemental distribution inside each particle is still unknown because the spatial resolution is almost the same as the particle sizes as mentioned before, it has been clarified that the element ratio of each particle inside the sample is almost the same. This result is consistent with the previous fluorescent X-ray imaging experiments of artificial diamond (Yamamoto *et al.*, 2000*b*; Ohigashi *et al.*, 2002). Wakatsuki *et. al.* (1982) showed that the

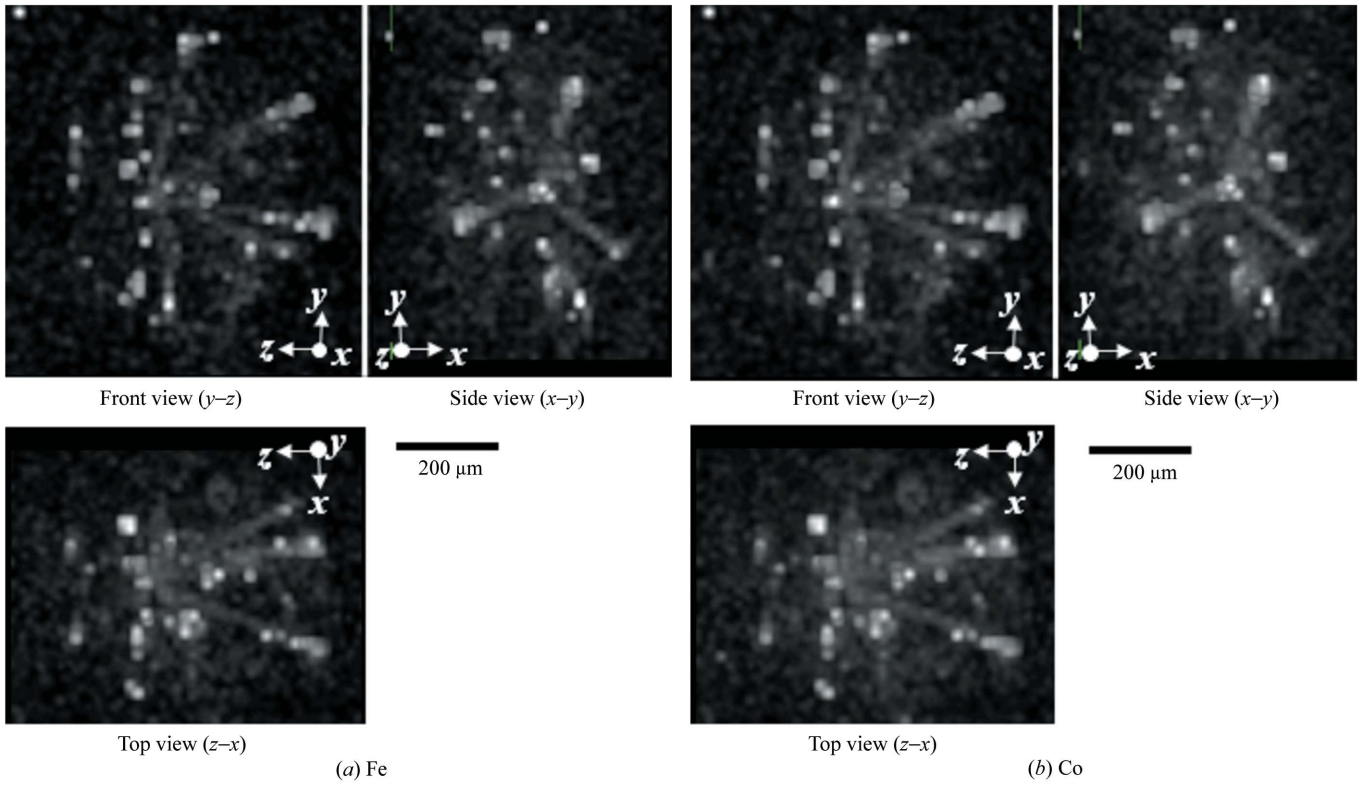

Figure 5
Energy-resolved three-dimensional X-ray fluorescence images of the artificial diamond. (*a*, *b*) Elemental mapping image of Fe and Co, respectively. The image data set consists of 150 sliced images with a translation scan pitch of 4 mm, and each sliced image consists of the integration of 300 photon-counting images. The exposure time for each photon-counting image is 1 s with the 1/40 intensity of full-power 'sheet-beam' X-rays of BL37XU. The photon incidence per CCD pixel per unit time was about 0.1 photons pixel^{-1} s^{-1} at maximum. The incident X-ray energy is 10 keV. Each image was taken in 4 × 4 binning mode of the CCD camera. The voxel size is 4 mm × 4 mm × 4 mm, and the number of voxels is 256 (*y*) × 256 (*z*) × 150 (*x*). The total measurement time was ∼55 h. (*c*) X-ray fluorescence spectrum derived from the histogram of the photon-counting image data set.

majority of several tens of particles selectively analyzed using an electron probe microanalyser had almost the same elemental ratio as the solvent alloy (Takano *et al.*, 1981). This suggests that every element may have almost the same distribution in the crystal, and the experimental result confirms this suggestion.

Because the system was not sophisticated enough for energy-dispersible imaging, it took a long time (∼55 h) for the measurement. About 75% of the measurement time was dead-time occupied by data readout and transfer of the CCD camera (∼3.5 s for each frame × 300 photon-counting images × 150 slices), and most of the other 25% was spent on the shutter response (∼1 s for each frame). Therefore, the throughput was restricted by these components; however, drastic shortening of the measurement time may be possible with only some minor improvements. For example, more than 1 Hz frame rate without statistic loss may be possible by decreasing the analogue-to-digital (A/D) conversion ratio of the CCD camera. In this experiment, the A/D conversion ratio was 14-bit. However, considering that the number of electrons (*N*) generated by photoelectric absorption of one X-ray photon with energy *E* (eV) is defined as $N = E/3.65$, an A/D ratio of 10–12-bit is suitable for the photon-counting mode. Even 8-bit is sufficient because the energy resolution of this method is several hundred eV. Finally, measurement within 1 h may be possible by upgrading with commercial equipment such as a high-speed detector and millisecond X-ray shutter.

This study has been performed under the approval of the SPring-8 Proposal Review Committee (PRC No. 2003B0138-NM-np).

References

Aoki, S., Takeuchi, A. & Ando, M. (1998). *J. Synchrotron Rad.* **5**, 1117–1118.
Golosio, B., Somogyi, A., Simonovici, A., Bleuet, P., Susini, J. & Lemelle, L. (2004). *Appl. Phys. Lett.* **84**, 2199.

Hoshino, M., Ishino, T., Namiki, T., Yamada, N., Watanabe, N. & Aoki, S. (2007). *Rev. Sci. Instrum.* **78**, 073706.
Kanngießer, B., Malzer, W. & Reiche, I. (2003). *Nucl. Instrum. Methods Phys. Res. B*, **211**, 259–264.
Ohigashi, T., Hoshino, M., Takeda, Y., Yamada, N., Namiki, T., Ishino, T., Watanabe, N. & Aoki, S. (2006). *IPAP Conf.* **7**, 154.
Ohigashi, T., Watanabe, N., Yokosuka, H. & Aoki, S. (2004). *AIP Conf. Proc.* **705**, 1352–1355.
Ohigashi, T., Watanabe, N., Yokosuka, H., Aota, T., Takano, H., Takeuchi, A. & Aoki, S. (2002). *J. Synchrotron Rad.* **9**, 128–131.
Onuki, T., Sugisaki, K. & Aoki, S. (1992). *Proc. SPIE*, **1720**, 258–263.
Suzuki, Y., Takeuchi, A. & Terada, Y. (2008). *Proceedings of the IEEE Nuclear Science Symposium*, Dresden, Germany, pp. 602–605.
Takano, K., Wakatsuki, M. & Shimomura, O. (1981). *High Pressure in Research and Industry*, edited by C. M. Backman *et al.*, p. 567. Uppsala: Arkitektopia.
Takeuchi, A., Aoki, S., Yamamoto, K., Takano, H., Watanabe, N. & Ando, M. (2000). *Rev. Sci. Instrum.* **71**, 1279.
Takeuchi, A., Suzuki, Y., Takano, H. & Terada, Y. (2005). *Rev. Sci. Instrum.* **76**, 093708.
Terada, Y. *et al.* (2004). *AIP Conf. Proc.* **705**, 376–379.
Tsunemi, H., Wada, M. & Hayashida, K. (1991). *Jpn. J. Appl. Phys.* **30**, 3540–3544.
Vekemans, B., Vincze, L., Brenker, F. E. & Adams, F. (2004). *J. Anal. At. Spectrom.* **19**, 1302–1308.
Wakatsuki, M. (1982). *J. Jpn. Assoc. Mineral. Petrol. Econ. Geol.* **3**, 143–151. (In Japanese.)
Wakatsuki, M. (1984). *Materials Science of the Earth's Interior*, edited by I. Sunagawa, pp. 351–374. Tokyo: Terra Scientific.
Watanabe, N., Yamamoto, K., Takano, H., Ohigashi, T., Yokosuka, H., Aota, T. & Aoki, S. (2001). *Nucl. Instrum. Methods Phys. Res. A*, **467–468**, 837–840.
Yamamoto, K., Watanabe, N., Takeuchi, A., Takano, H., Aota, T., Fukuda, M. & Aoki, S. (2000*a*). *J. Synchrotron Rad.* **7**, 34–39.
Yamamoto, K., Watanabe, N., Takeuchi, A., Takano, H., Aota, T., Kumegawa, M., Ohigashi, T., Tanoue, R., Yokosuka, H. & Aoki, S. (2000*b*). *AIP Conf. Proc.* **507**, 259–262.